

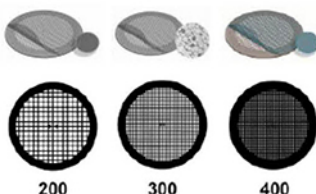
Nanocharacterization by TEM and AFM

We offer a wide range of TEM and AFM tools, from TEM grids and finders to AFM substrates and grippers.

Available in a wide variety of designs and materials to support your work, select from a broad range of mesh sizes, specimen supporting films, and materials that perfectly suit the conditions of your TEM analysis.

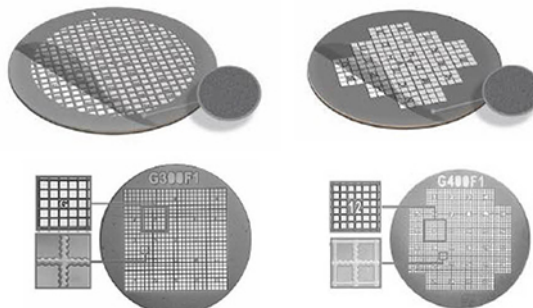
TEM grid specifications:

Material	Mesh Size and Shape	Film Specifications
<ul style="list-style-type: none"> • Cu • Ni • Au • Mo • Cu/Pd 	<ul style="list-style-type: none"> • Square or hexagonal • Single-hole grid (75 mm or 100 mm) • 100 • 150 • 200 • 300 • 400 	<ul style="list-style-type: none"> • None • Continuous formvar film (thicknesses: 5-6 nm, 10 nm) • Lacey carbon film (average hole sizes: 50 nm, 100 nm, 150 nm, 100 nm, 150 nm) • Continuous amorphous carbon film (thicknesses: 10 nm, 20-30 nm) • Continuous formvar/carbon film (thickness: 10nm formvar and 1nm carbon)



TEM finder grid specifications:

Material	Mesh Size	Film Specifications
<ul style="list-style-type: none"> • Cu • Ni • Au 	<ul style="list-style-type: none"> • 135 • 200 • 300 • 400 	<ul style="list-style-type: none"> • None • Continuous amorphous carbon film (thicknesses: 3-4 nm, 10 nm, 20-30 nm)



Supporting Tools for Nanomaterial Characterization

Our comprehensive range of supporting materials for nanomaterial characterization includes tweezers (sharp tip, disc gripper for AFM), TEM window grids (various thicknesses, 1 or 9 windows), a magnetic pick-up tool, a grid storage box, cryo-capsules, lift-out grids (Cu or Mo), AFM substrates (various dimensions), and much more.



Explore our complete range of TEM grids on:
[SigmaAldrich.com/nanocharacterization](https://sigmaaldrich.com/nanocharacterization)

© 2022 Merck KGaA, Darmstadt, Germany and/or its affiliates. All Rights Reserved. Merck, the vibrant M, and Sigma-Aldrich are trademarks of Merck KGaA, Darmstadt, Germany or its affiliates. All other trademarks are the property of their respective owners. Detailed information on trademarks is available via publicly accessible resources.

MK_AD9792EN 43729 08/2022

The Life Science business of Merck operates as MilliporeSigma in the U.S. and Canada.

Sigma-Aldrich®
 Lab & Production Materials

Enhanced Thermal Stability of Low-Temperature Processed Carbon-Based Perovskite Solar Cells by a Combined Antisolvent/Polymer Deposition Method

Soe Ko Ko Aung, Anuja Vijayan, Gerrit Boschloo,* and Tosawat Seetawan*

Low-temperature processed carbon-based perovskite solar cells have received great attention due to low-cost, high stability, and simple preparation processes that can be employed in large-scale manufacturing. Carbon paste is deposited by techniques such as doctor blading or screen printing. However, solvents from this paste can damage the perovskite or underlying layers resulting in poor performance of solar cells. Furthermore, carbon is not an ideal hole-selective contact. To overcome these issues, the antisolvent treatment is combined with the deposition of a polymeric hole conductor. Specifically, poly(3-hexylthiophene) (P3HT), added into the chlorobenzene antisolvent, improves perovskite morphology and reduces interfacial carrier recombination. As a result, the power conversion efficiency (PCE) of solar cells with the device structure $\text{SnO}_2/\text{MAPbI}_3/\text{P3HT}/\text{carbon}$ increases to 12.16% from 10.6% of pristine devices without P3HT, using pure antisolvent. For poly(triarylamine) hole conductor in the same method, PCE improves only slightly to 11.1%. After 260 h of thermal stress at 82 °C, the P3HT-additive devices improve PCE up to 13.2% in air and maintain 91% of their initial efficiency over 800 h.

1. Introduction

Organic–inorganic hybrid perovskite solar cells (PSCs) have attracted tremendously owing to their outstanding optoelectronic

properties,^[1–4] and low-temperature (LT) solution processing.^[5,6] Thus, power conversion efficiency (PCE) of PSC has rapidly increased up to 25.7% in 2021^[7] being comparable to Si and better than existing thin film solar cells technologies, making PSC of high interest for low-cost photovoltaic applications.^[8] However, the insufficient long-term stability of PSCs based on lead halides perovskites hinders commercialization at this point. Perovskite decomposition is mostly due to the loss of organic components and formation of iodine due to environmental effects of thermal, humidity, and light condition.^[9,10] Highest efficiencies for PSCs are obtained using the n–i–p structure, where the p-type contact is the widely used hole-transport material (HTM), 2,20,7,7'-tetrakis [N,N-di(4-methoxyphenyl)amino]-9,9'-spirobifluorene (spiro-OMeTAD). For good performance, it is essential to dope the

spiro-OMeTAD with the hygroscopic salt lithium bis(trifluoromethane)sulfonimide (LiTFSI) and the volatile 4-*tert*-butylpyridine (tBP), which are detrimental for the stability of the PSCs.^[11,12] Moreover, metal contacts, such as gold (Au) and silver (Ag), are normally deposited using vacuum evaporation on top of the HTM, which is expensive and requires much energy. Furthermore, these metals react with halide ions from the perovskite within the spiro-OMeTAD layer, giving rise to degradation at elevated temperatures.^[13,14]

Fortunately, alternative electrodes based on carbon materials, such as carbon nanotubes (CNTs), graphene, graphite, and carbon black, appear to be much more stable and were successfully applied in PSCs.^[15–17] With the trend toward low-cost and large-scale fabrication, carbon electrodes are promising candidates to replace metal electrodes because of suitable work function (−5.0 eV), vacuum free deposition, ultralow cost, and hydrophobicity, leading to long-term stability of PSCs.^[18,19] In 2013, the monolithic PSC structure composed of scaffolds of $\text{TiO}_2/\text{ZrO}_2/\text{carbon}$ was first used, where perovskite is introduced by drop-casting precursor solution on the top of mesoscopic carbon layer, and a PCE of 6.6% was achieved.^[20] To date, printable, HTM-free C-PSCs increased efficiency up to 17.47% after P5PEAI posttreatment by tuning the energy band alignment.^[21] However, the typical multilayer mesoporous structure requires a high-temperature annealing step ($\geq 450^\circ\text{C}$), which prevents the use of flexible polymer substrates and increases the energy pay-back time.^[22,23]

S. K. K. Aung, T. Seetawan
Department of Physics
Faculty of Science and Technology
Optic Research Laboratory
Center of Excellence on Alternative Energy
Research and Development Institute
Sakon Nakhon Rajabhat University
47000 Sakon Nakhon, Thailand
E-mail: t_seetawan@snru.ac

S. K. K. Aung, A. Vijayan, G. Boschloo
Department of Chemistry—Ångström-Laboratory
Physical Chemistry
Uppsala University
SE-751 20 Uppsala, Sweden
E-mail: gerrit.boschloo@kemi.uu.se

The ORCID identification number(s) for the author(s) of this article can be found under <https://doi.org/10.1002/ente.202200177>.

© 2022 The Authors. Energy Technology published by Wiley-VCH GmbH. This is an open access article under the terms of the Creative Commons Attribution-NonCommercial License, which permits use, distribution and reproduction in any medium, provided the original work is properly cited and is not used for commercial purposes.

DOI: 10.1002/ente.202200177

To address these drawbacks, LT ($\leq 180^\circ\text{C}$) processed C-PSCs were developed with electron transport layers (ETLs) such as SnO_2 ^[24,25] and ZnO .^[26,27] Among them, SnO_2 is of great interest for alternative ETL owing to wide bandgap ($>3.6\text{ eV}$), energy matching with perovskite, high carrier mobility ($240\text{ cm}^2\text{ V}^{-1}\text{ s}^{-1}$) as well as excellent stability under the UV light.^[28–30] In contrast, the hydroxyl groups in the ZnO surface causes the degradation of perovskite layer due to proton-transfer reactions at the interface between perovskite and ZnO .^[31,32] On the other hand, hydrophobic materials (such as PTAA, PEDOT:PSS, and P3HT) are alternative HTMs to protect the moisture corrosion of devices. Among them, P3HT appears to be a promising hole conductor toward PSC commercialization due to its high hole mobility ($0.1\text{ cm}^2\text{ V}^{-1}\text{ s}^{-1}$), low cost, robust hydrophobicity, excellent thermal stability, and temperature tolerance (100 and -80°C).^[33–35]

Chu et al. developed the LT processed C-PSCs with poly(3-hexylthiophene-2,5-diyl) (P3HT)/graphene composite hole transport layer (HTL) achieved a recorded efficiency of 17.8% from 11.1% for pristine P3HT.^[36] In our recent work, we inserted undoped P3HT between carbon and perovskite (MAPbI_3), which led to devices with a PCE of 15.7% that maintained 70% of its initial performance for 900 h at 82°C in air.^[37] In other recent work, 2,3,5,6-tetrafluoro-7,7,8,8-tetracyanoquinodimethane (F4TCNQ) was added into the perovskite of a device with undoped P3HT/carbon, leading to an enhanced PCE of 15.1% due to improved energy level matching.^[38]

To date, the highest efficiency of 24.6% was achieved when gallium (iii) acetylacetonate ($\text{Ga}(\text{acac})_3$) was incorporated into the P3HT/Au device, showing the superior stability in air for 2000 h.^[39] Jin et al. reported that ZnO -based C-PSC device reached efficiency up to 16.05% when P3HT was inserted between perovskite and carbon leading to suitable energy alignment and retained its initial efficiency over 90% for 1200 h in air.^[26]

Conventional methods for depositing the carbon paste on the perovskite film, such as screen printing or doctor blading, can damage the underlying layer and lead to poor interfacial contact. Hence, several methods are reported to solve back-interface problems in carbon electrodes using free-standing method,^[40] solvent-exchange and hot pressing,^[41–45] heat gun annealing,^[46] and scribing method.^[47] Zhou et al. removed the corrosive

solvent present in commercial carbon paste chlorobenzene (CB) to avoid damaging the underlying layer.^[48] Behrouznejad et al. prepared a suitable carbon paste with CB solvent from scratch.^[49] A combined antisolvent/polymer hole conductor deposition was introduced by Han *et al.* by dissolving poly[bis(4-phenyl)(2,4,6-trimethylphenyl)amine] (PTAA) in the CB used as an antisolvent method. The polymer induced more columnar perovskite crystals and created a slight gradient of PTAA in the perovskite, referred to as gradient bulk heterojunction, while most of the PTAA is forming a film on top. The resulting C-PSCs gave efficiencies up to 13.0%.^[50] Very recently, the same method was applied in C-PSC using P3HT, achieving a PCE of 14.3%^[51] and 15.57%.^[52]

In our study, we use a similar approach: C-PSC devices are prepared in all LT process ($\approx 150^\circ\text{C}$) using P3HT or PTAA diluted in the CB antisolvent. As-prepared MAPbI_3 -P3HT/carbon devices achieved a good PCE of 12.16% while PTAA-added devices gave 11.11% and devices with pure antisolvent 10.6%. Moreover, its efficiency was enhanced up to 13.24% for 264 h after thermal stress at 82°C in air, and subsequently retained 91% of its initial PCE for 864 h (without encapsulation). Electrochemical impedance spectroscopy (EIS) indicates that interfacial recombination rate is significantly reduced by addition of P3HT perovskite film.

2. Results and Discussion

Absorption spectra of perovskite films with and without (w/o) polymeric HTM additives are observed in **Figure 1a**. The absorbance of PTAA-additive films is not changed in the wavelength 800–500 nm compared with the pristine film.^[50] For P3HT-additive films, a higher absorbance value in the range between 725 and 500 nm is found compared to the other films. This can be attributed to the absorption by the colored P3HT polymer. Based on this absorbance (≈ 0.2), a rough estimate of the thickness of the P3HT of 40 nm can be made. The Tauc plot (inset in **Figure 1a**) shows that the absorption onset of all films is identical, corresponding to a bandgap of 1.61 eV. The bandgap is determined by applying Tauc analysis using the following equation,^[53]

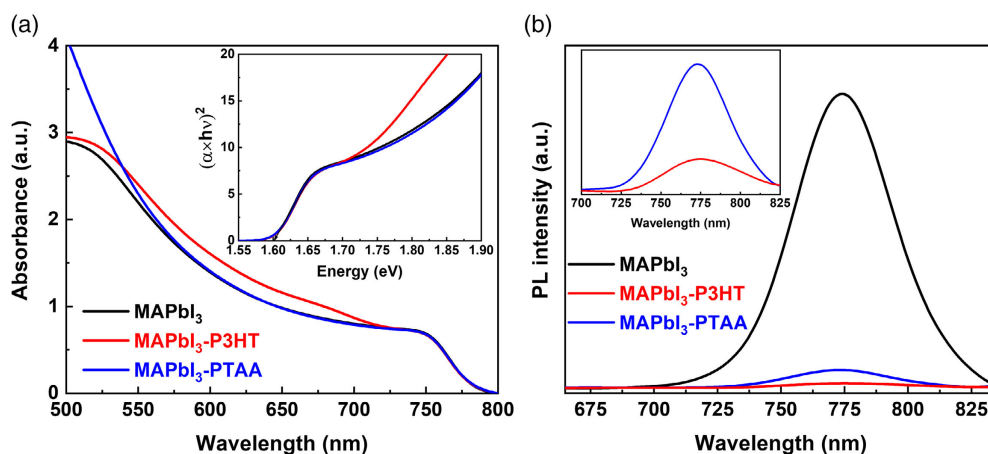


Figure 1. a) UV-vis absorption spectra with and without additive polymeric films. Inset shows the Tauc plot confirmed a bandgap of 1.61 eV. b) PL spectra of the pristine MAPbI_3 film and polymer-additive films (P3HT and PTAA) upon excitation at a wavelength of 460 nm.

$(\alpha h\nu)^2 = C(h\nu - E_g)$, where α is the absorption coefficient, h is Planck's constant, ν is the frequency of light, E_g is the energy bandgap, and C is a proportionality constant.

Steady-state photoluminescence (PL) spectra are further performed through the excitation on the front side of perovskite/ITO substrates as shown in Figure 1b. The strong PL emission peak at 770 nm (1.61 eV) is assigned to radiative band-to-band carrier recombination in the MAPbI₃ film^[54] and is in excellent agreement with the Tauc-plot determination. In the P3HT- and PTAA-additive perovskite films, PL intensities are significantly reduced. This quenching is caused by efficient hole extraction from MAPbI₃ to the hole conductor.^[50,55] Compared to PTAA-additive films, P3HT-additive film shows stronger PL quenching (see inset in Figure 1b), suggesting faster hole transfer from perovskite to the HTM.

Scanning electron microscopy (SEM) is used to characterize the morphology of the films. A distinct difference is found between perovskite films with and without polymer additives (see Figure 2). Without polymer additives, the MAPbI₃ perovskite film displays a rather large variation of grains, ranging from 100 nm to 1.2 μ m. Importantly, significant cracks are observed at the grain boundaries between large grains in the pristine film in some places. With P3HT additive such cracks are not found and a more uniform surface is observed. There appears to be a thin and homogeneous P3HT layer on top of the perovskite. The grains in the perovskite are still partially visible underneath, and seem to be more uniform in size. In contrast, in PTAA-additive films the polymer coverage is a less uniform and a higher surface roughness can be seen (Figure 2c). The flexible nature of the introduced polymer may be the reason that cracks can be avoided upon cooling the film after the annealing procedure.

The statistical grain size distributions of pristine and P3HT-additive MAPbI₃ films are shown in Figure S7, Supporting

Information. The average grain size in pristine MAPbI₃ film (443 ± 243 nm) is larger while the size distribution is much broader than that of P3HT-additive film (303 ± 54 nm). The more uniform nature of the modified perovskite film is important for pinhole-free devices and for future up-scaling. The smaller grain size for P3HT-added perovskite films could originate from the chemical interaction of the thiophene groups with the perovskite precursors, directly influencing the perovskite grain and film formation. In previous work it has been demonstrated that thiophene molecules can passivate the surface of lead halide perovskite through their interaction as a Lewis base.^[56]

X-Ray diffraction (XRD) results show that the P3HT-additive MAPbI₃ films are highly crystalline, with the strongest diffraction peak (2θ) at 14.1° higher in intensity than that of pristine films (see Figure S1, Supporting Information).

The polar nature of the exposed surface was investigated using water contact angle measurements (see Figure 3). The pristine MAPbI₃ perovskite film displays a contact angle of about 56° , demonstrating that the surface is rather polar. Contact angles of perovskite films with polymeric additives were much larger ($\approx 101^\circ$), which can be attributed to the hydrophobic nature of P3HT and PTAA, which are covering the surface. A hydrophobic surface is favorable for improved stability of the films in the presence of water.

Figure 4a shows the schematic diagram for the preparation of C-PSC with the combined antisolvent/polymer deposition method films, where two spin coating steps are used, for perovskite deposition and for antisolvent/polymer deposition, and a doctor blading step for the carbon electrode. The same amount of P3HT or PTAA (2.5 mg mL^{-1}) is diluted in CB for the polymer-additive perovskite films. Finally, carbon paste (Dyename DN CP-01, sheet resistance $\approx 10 \Omega \square^{-1}$) is directly deposited on the with and w/o additive polymeric perovskite

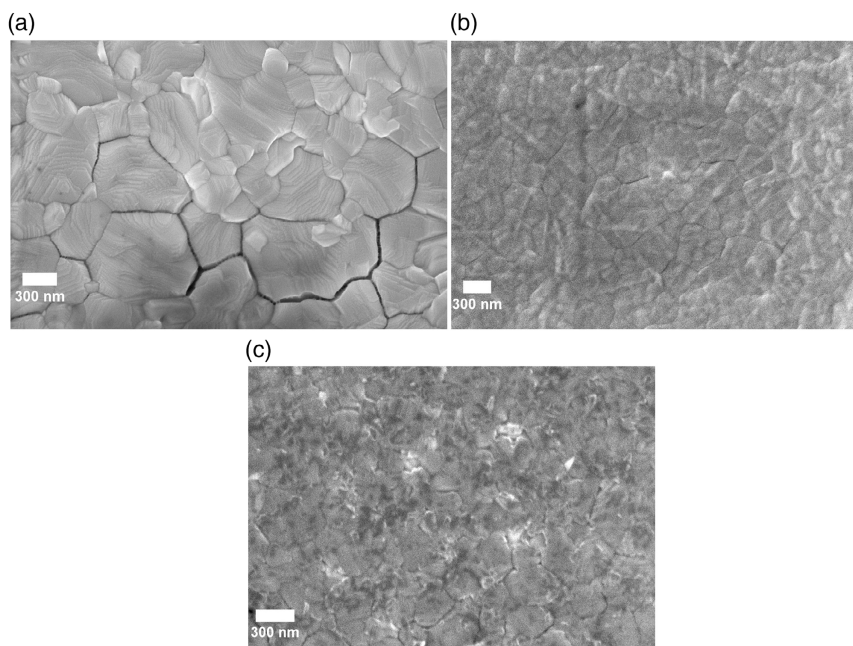


Figure 2. Top-view SEM images of a) pristine MAPbI₃, b) P3HT-additive MAPbI₃, and c) PTAA-additive MAPbI₃ surfaces.

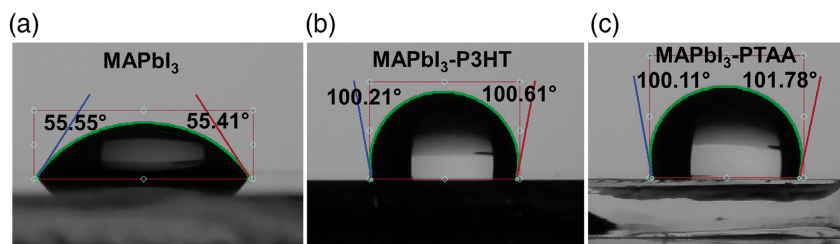


Figure 3. Water contact angle measurements of perovskite films with and without polymer additives: a) pristine MAPbI₃, b) MAPbI₃-P3HT, and c) MAPbI₃-PTAA.

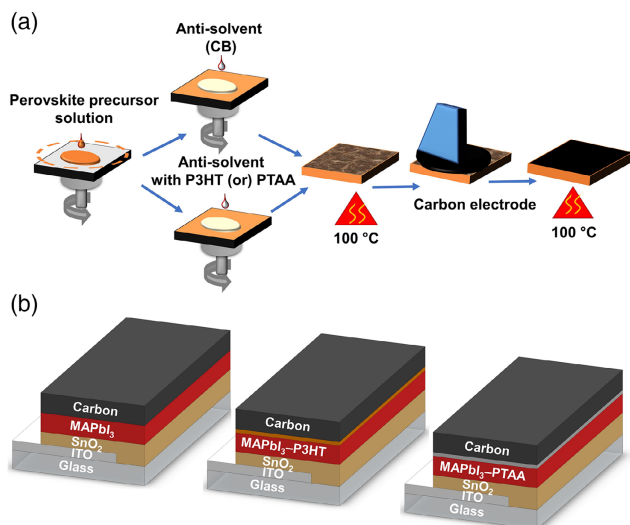


Figure 4. a) Schematic diagram with and w/o polymer-additive antisolvent perovskite films and carbon electrode deposition. b) n-i-p planar type C-PSCs: pristine MAPbI₃ and MAPbI₃ with P3HT or PTAA additive.

films. Three different n-i-p device architectures for ITO/SnO₂/MAPbI₃/carbon, ITO/SnO₂/MAPbI₃-P3HT/carbon, and ITO/SnO₂/MAPbI₃-PTAA/carbon are shown in Figure 4b.

Photovoltaic performance for fresh pristine MAPbI₃ and with and w/o polymeric films is displayed in Figure 5a. The corresponding photovoltaic parameters measured under 100 mW cm⁻² AM1.5 G illumination are summarized in Table 1. The pristine MAPbI₃/carbon device shows a PCE of 10.61%, fill factor (FF) of 61.76%, short-circuit current density (J_{SC}) of 20.87 mA cm⁻², and open-circuit voltage (V_{OC}) of 0.823 V. In additive P3HT films, PCE is significantly improved to 12.16%, FF of 63.59%, J_{SC} of 21.58 mA cm⁻², and V_{OC} of 0.886 V. Consistently, average FF increases from 58.87 ± 1.73% (pristine) to 62.86 ± 1.53% (MAPbI₃-P3HT). The average V_{OC} for pristine and additive P3HT devices was 0.841 ± 0.02 and 0.87 ± 0.013 V, respectively. The enhanced PCE mainly comes from the improvement in FF. P3HT can passivate the perovskite, reducing defects at interfaces,^[5] while the improved hole selectivity of P3HT-added perovskite-carbon contacts will also improve the FF.

PTAA-additive device showed a PCE of 11.11% with FF of 58.75%, V_{OC} of 0.890 V, and J_{SC} of 21.23 mA cm⁻². The average V_{OC} is significantly higher than that of pristine MAPbI₃ to 0.89 ± 0.01 V, ascribed improved charge separation due to the

added HTM. However, an average FF of 55.68 ± 2.35% is lower than the pristine device, suggesting that it does not improve the film quality much and may have a relatively poor contact with the carbon electrode.

We further investigate the stabilized maximum power point (MPP) output for devices with and w/o polymeric additive under 1 sun illumination in air (see Figure 5b). In particular, P3HT-additive device achieved a higher stabilized PCE of 11.54% within 350 s compared to the pristine device (10.39%) and PTAA-additive device (10.51%). Stabilized current density for pristine and P3HT-additive device is similar, with values of 20.9 mA cm⁻². However, for PTAA device a slightly lower value of 20.7 mA cm⁻² was observed. Figure 5c illustrates the energy band diagram of the C-PSCs with pristine and polymer-added MAPbI₃. The highest occupied molecular orbital (HOMO) levels of P3HT and PTAA values are suitably matched in energy with the valence band maximum (VBM) of the perovskite and the Fermi level of carbon electrode.

The statistical distribution of solar cell parameters of devices with pure and P3HT- and PTAA-added antisolvent can be seen in Figure S2, Supporting Information. The statistic results confirm that for P3HT-additive devices FFs are significantly higher than that of pristine MAPbI₃ and MAPbI₃-PTAA/carbon devices. While lowest FFs are found for (MAPbI₃-PTAA), these devices display higher V_{OC} than the other device structures.

Increasing the concentration of P3HT and PTAA from 2.5 to 5 mg mL⁻¹ yielded average PCE values of 11.15 ± 0.50% for (MAPbI₃-P3HT) and 10.79 ± 0.51% for (MAPbI₃-PTAA) devices. No distinct improved was found compared with aforementioned results (see details in Figure S3, Supporting Information).

The enhanced efficiency of devices with P3HT additive can be mainly attributed to the increase of FF. Analysis of the J - V curves shows that it is related to a high shunt resistance (R_{SH}) and short-circuit current density (J_{SC}) (see Table 1). The series resistance (R_S) and shunt resistance (R_{SH}) could be determined using the following equation:^[57,58] $-\frac{dV}{dJ} = \frac{AK_B T}{e} (J_{SC} - J)^{-1} + R_S$, where R_S is the series resistance, V is the bias voltage applied for the cells, J is the current density, A is the diode ideality factor, K_B is the Boltzmann's constant, T is the absolute temperature, and e is the charge of electron. The R_S value could be estimated from the linear relationship between $-\frac{dV}{dJ}$ and $(J_{SC} - J)^{-1}$. The R_{SH} value could be obtained when V is close to zero by the following equation: $-\frac{dV}{dJ} = R_{SH}$. Indeed, average R_{SH} for MAPbI₃-P3HT/carbon devices is 1842 ± 382 Ω cm², which is about 3.5 times higher than that of 513 ± 142 Ω cm² (MAPbI₃/carbon)

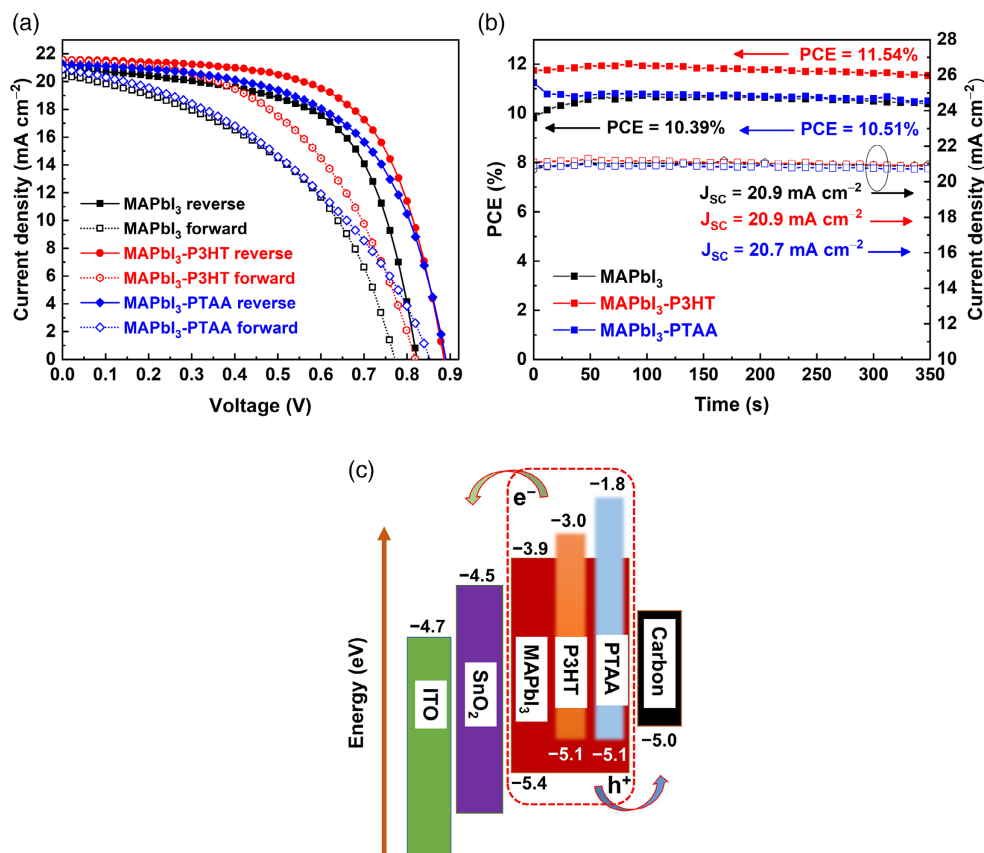


Figure 5. a) *J*-*V* curves with hysteresis behavior of best performing fresh devices; b) steady-state PCE and *J*_{sc} measured during MPP tracking of C-PSCs in air under AM1.5 G illumination; c) energy band diagram of C-PSC with the optional polymer additives (P3HT or PTAA).

Table 1. Photovoltaic parameters of fresh devices in one batch (ten of each type) based on MAPbI₃ perovskite with and w/o P3HT and PTAA additives in the CB antisolvent.

Devices	PCE	FF	<i>J</i> _{sc}	<i>V</i> _{oc}	<i>R</i> _{SH}	<i>R</i> _s	HI
	[%]	[%]	[mA cm ⁻²]	[V]	[Ω cm ²]	[Ω cm ²]	
MAPbI ₃	10.61	61.76	20.87	0.823	525.56	5.24	0.184
Average	10.33	58.87	20.86	0.841	513.18	5.85	0.164
	±0.38	±1.73	±0.19	±0.02	±142	±0.83	±0.016
MAPbI ₃ -P3HT	12.16	63.59	21.58	0.886	1523.29	5.64	0.154
Average	11.63	62.86	21.25	0.870	1842.00	5.63	0.166
	±0.43	±1.53	±0.18	±0.013	±382.41	±0.5	±0.01
MAPbI ₃ -PTAA	11.11	58.75	21.23	0.890	860.31	6.32	0.203
Average	10.38	55.68	20.99	0.89	525.71	7.30	0.171
	±0.61	±2.35	±0.09	±0.01	±156.53	±0.53	±0.009

and 525 ± 156 Ω cm² (MAPbI₃-PTAA/carbon) devices listed in Table 1. Moreover, average the series resistance (*R*_s) of P3HT-additive device (5.63 ± 0.5 Ω cm²) is slightly lower than that of pristine device (5.85 ± 0.83 Ω cm²). However, PTAA-additive device (7.3 ± 0.53 Ω cm²) showed a relatively high series resistance, leading to the lower FF (see Table 1).

We investigated the hysteresis in *J*-*V* curves by analyzing the hysteresis indices (HI) calculated by the formula^[37]

$$HI = \frac{PCE^- - PCE^+}{PCE^- + PCE^+} \quad (1)$$

where - and + were the PCE from reverse and forward scans, respectively. Similar average hysteresis index (HI) values for 0.164 ± 0.016 (pristine), 0.166 ± 0.01 (P3HT), and 0.171 ± 0.009 (PTAA) can be observed (see Table 1). The schematic diagram for interfacial contacts of these carbon devices can be seen in Figure S4, Supporting Information.

We further investigated the *V*_{oc} decay between the three types of devices, as shown in Figure 6a. Under illumination of the devices under open circuit, positively and negatively charged defects will move toward and accumulate at the electron-selective electrode (SnO₂) and hole-selective electrode (carbon), respectively. In the dark period, these defects will slowly move back to their equilibrium state, which causes a relatively slow *V*_{oc} decay. The decay of PTAA-MAPbI₃ devices is slower than that of pristine MAPbI₃. However P3HT-MAPbI₃ have by far the largest slow part in the *V*_{oc} decay transient. This suggests that the polymer-added devices allow for more ion accumulation near the carbon electrode than the pristine devices. It appears that

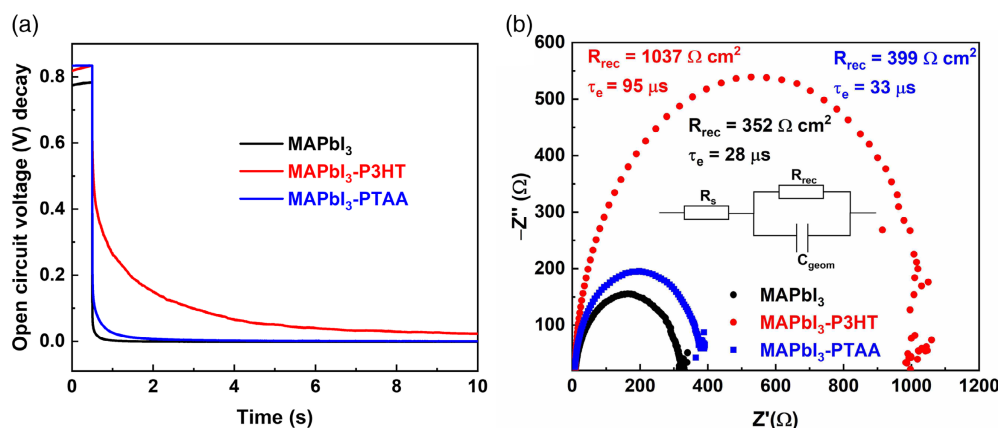


Figure 6. a) Open-circuit voltage (V_{OC}) decay measurement after 1 sun illumination for 0.5s. b) Impedance spectroscopy: Nyquist plot of pristine and P3HT- and PTAA-added devices, measured at a bias voltage of 0.8 V under the dark within the frequency range from 500 kHz to 1 Hz.

iodide ions might be inserted into the P3HT layer under illumination conditions.

To confirm these results, EIS was conducted to further analyze the interfacial charge extraction and recombination behavior of C-PSCs (see Figure 6b). In the Nyquist plots, the high-frequency intercept gives the series resistance (R_s) mainly from the ITO and carbon conducting layers, while at lower frequencies a semi-circle is found due to the recombination resistance (R_{rec}) and the geometric capacitance of the device.^[25,59] Fitted parameters using equivalent circuit from Nyquist plots are given in Table S1,

Supporting Information. R_s values of P3HT and PTAA-added/carbon devices are 7.32 and 7.59 Ω, slightly lower compared with that of pristine MAPbI₃/carbon device (8.32 Ω). Furthermore, the P3HT-added device has significantly higher R_{rec} (1037 Ω) than that of PTAA (399 Ω) and pristine (352 Ω) devices, leading to less recombination at the interfaces. Consequently, the highest R_{rec} and lowest R_s values of MAPbI₃-P3HT/carbon device can offer the higher V_{OC} and FF, which are consistent with the V_{OC} decay measurement and $J-V$ curves. Furthermore, carrier lifetime (τ) can be calculated by using the following formula: $\tau = R_{rec} \times C_{geom}$.

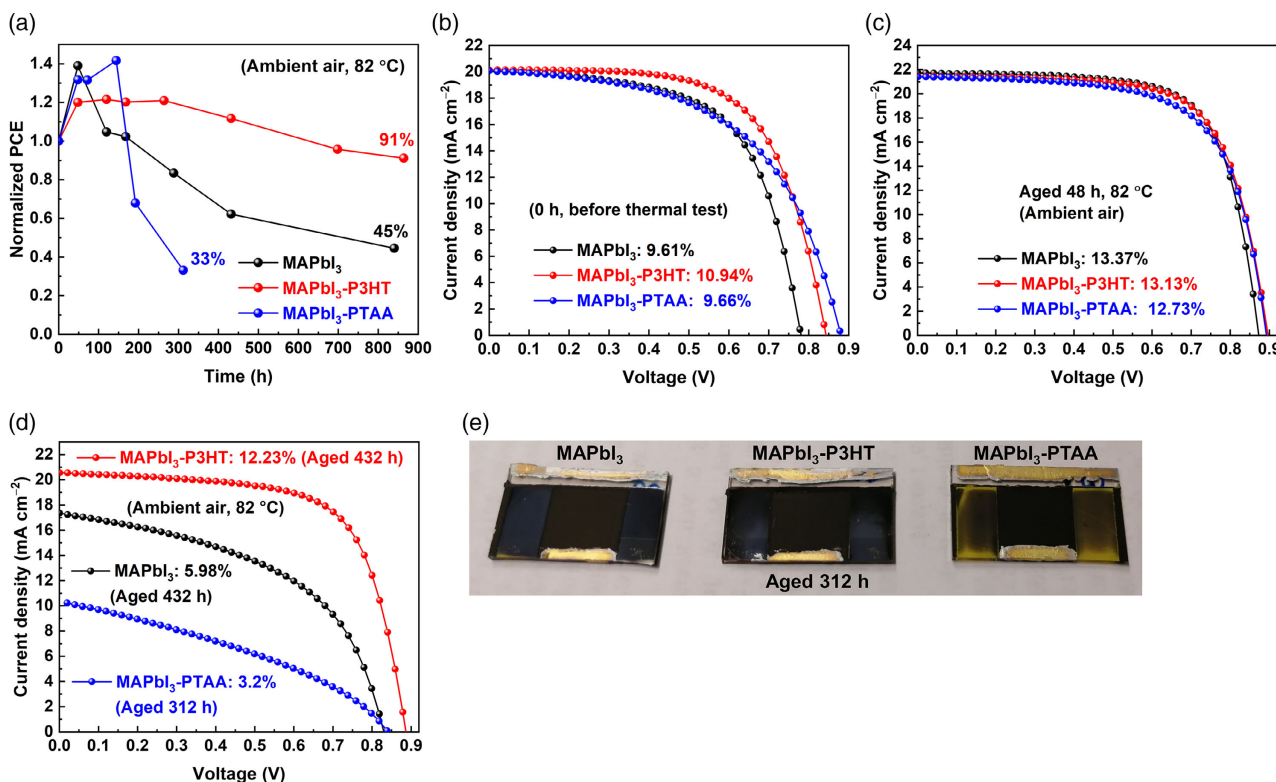


Figure 7. a) Thermal aging tests at 82 °C in air. Unencapsulated devices were baked under the dark; b) 0 h, c) 48 h, and d) 312 h for PTAA and 432 h for pristine- and P3HT-added device. e) The degradation of PTAA additive perovskite layer after storage for 312 h at 82 °C in air.

Calculated τ values of pristine-, P3HT-, and PTAA-additive devices are 28, 95, and 33 μ s, respectively. The longer carrier lifetime for the P3HT-added devices indicates the more efficient separation of electrons and holes in the device.

Furthermore, the thermal stability of unencapsulated solar cell devices was evaluated by storing in darkness in an oven (in ambient air, RH $\approx 40 \pm 10\%$ in the lab) (see Figure 7a). After thermal stress at 82 °C for 48 h, all devices showed improved efficiencies up to $\approx 13\%$ (see Figure 7c). This can be attributed to evaporation of residual solvents in the carbon electrode during the heat test, leading to improved conductivity of the electrodes and possibly improved contact between perovskite and carbon electrodes. The former can explain the improved FF, which is largely due to reduced series resistance. In a separate test, we confirmed that the sheet resistance of carbon films on a glass substrates decreased from about 26 to 20 $\Omega \text{ sq}^{-1}$ after 48 h thermal stress. In addition, it is possible that the MAPbI₃ film improves in quality due to further crystallization and evaporation of residual DMSO. This was confirmed by the increase in MAPbI₃ photoluminescence after thermal stress in a separate test (see Figure S8, Supporting Information). This can explain the increase in photocurrent in the thermally stressed devices. The PTAA device improved its efficiency from 9.7% to 13.69% after 144 h. Then, its PCE rapidly dropped to 3.2% after storage for 312 h (see Figure 7d). The color of the perovskite with PTAA additive layer changed from dark brown to pale yellow, due to decomposition of the perovskite, presumably to PbI₂, as shown in Figure 7e. In contrast, the color of pristine and additive P3HT perovskite remained unchanged at this point. After 840 h, the pristine MAPbI₃/carbon device gave 45% of its initial efficiency because of lowering of FF and J_{SC} (see Figure S5, Supporting Information). In particular, MAPbI₃-P3HT/carbon devices improved their efficiency to 13.24% after 260 h of heat test, followed by a decrease to 12.23% after 432 h and to 9.97% after 864 h, maintaining 91% of its initial efficiency (75% of its top efficiency) (see Table S3, Supporting Information).

3. Conclusion

We successfully prepared LT processed carbon-based perovskite solar cells, using a combined antisolvent treatment/polymeric hole conductor deposition. Specifically, poly(3-hexylthiophene) added into the CB antisolvent was found to be suitable: it improved perovskite morphology, reduced interfacial recombination, and improved device stability. The PCE of solar cells with the device structure SnO₂/MAPbI₃/P3HT/carbon was boosted and the procedure led to significantly improved stability in a long-term heat stress test at 82 °C.

Combining the antisolvent treatment with hole conductor deposition is a useful strategy in perovskite solar cell preparation as it reduces the number of preparation steps and appears to have positive effects on the quality of the perovskite film as well.

4. Experimental Section

Materials: Indium tin oxide (ITO)-coated glasses (15 $\Omega \text{ sq}^{-1}$, Optical Filters, UK), tin (IV) oxide (SnO₂, 15% in H₂O colloidal dispersion, Alfa Aesar), methylammonium iodide (MAI, 99.99%, Greatcell Solar), lead

(II) iodide (PbI₂, 99.99%, TCI), *N,N*-dimethylformamide (DMF, anhydrous, 99.8%), dimethylsulfoxide (DMSO, anhydrous, 99.8%), CB (anhydrous, 99.8%), poly[bis(4-phenyl)(2,4,6-trimethylphenyl)amine] (PTAA, average M_n 7000–10 000, prod no. 702 471), and poly(3-hexylthiophene-2,5-diyl) (P3HT, regioregular, average M_w 50 000–100 000, prod no. 445 703) were purchased from Sigma-Aldrich. Commercial carbon paste (DN-CP01) was obtained from Dyenamo. All solvents and chemicals were used directly without further purification.

Solar Cell Preparation: ITO-coated glass substrates (28 \times 24 mm²) were etched with Zn powder and 2 M HCl diluted in water to form two detached electrode patterns. The substrates were ultrasonically cleaned using 2% Hellmanex with deionized water, acetone, and ethanol for 30 min in each step, and then dried by air stream. And the substrates were further treated by UV-ozone for 30 min. Then, SnO₂, nanoparticle colloid solution was diluted by deionized water (DI), with 1:4 (SnO₂:DI) volume ratio followed by sonication for 15 min before use. As-prepared solution was spin-coated on the ITO substrate at 3000 rpm for 30 s, and then annealed 150 °C for 30 min under ambient air. After cooling down to room temperature (RT), SnO₂-coated substrates were further cleaned by UV-ozone for 20 min. Thereafter, the clean substrates were quickly transferred to the N₂-filled glove box. The perovskite precursor solution was prepared by dissolving 239 mg of MAI and 692 mg of PbI₂ in a mixed solvent of 0.107 mL DMSO and 0.953 mL *N,N*-dimethylformamide (DMF)^[37] and it was stirred at 60 °C overnight under the dark at Ar glove box. The resultant mixture was filtered through a 0.45 μ m PTFE filter. Then, perovskite precursor solution was dropped on the SnO₂/ITO film, followed by spin coating at 4000 rpm for 20 s. During the spinning time between 7 and 10 s, 150 μ L of CB was dripped at the center of the substrate for pristine device. For PTAA- and P3HT-additive perovskite films, 2.5 mg of each amount was diluted in the 1 mL of CB, and then used an antisolvent procedure as well. Afterward, all samples were heated at 100 °C for 30 min to obtain the brilliant shining films. Unless noted otherwise, spincoating and annealing were performed under nitrogen atmosphere. Finally, Dyenamo carbon paste was deposited on the perovskite layer by doctor blading and then annealed on the hotplate at 100 °C for 20 min in ambient air (RH $\approx 40 \pm 10\%$, RT $\approx 25 \pm 5\%$).

Characterization: Current–voltage measurements were recorded using a self-calibrating Sinus-70 solar simulator (Wavelabs, Leipzig, Germany) and a source meter (Ossila X200, UK) under AM1.5 G illumination (100 mW cm⁻²) with reverse scan from +1.05 to -0.1 V and forward scan from -0.1 to 1.05 V, a scan rate at 50 mVs⁻¹. The active area of C-PSC was illuminated through the circular metal mask of 0.125 cm². UV–vis absorption spectra were measured by a UV–vis–NIR spectrophotometer (Varian Cary 5000). XRD measurements were characterized using a Rigaku (SmartLab) diffractometer with Cu K α ($\lambda = 1.54051 \text{ \AA}$) over the 10°–60° range with a step of 0.02°. Top-view SEM images were recorded using a Zeiss LEO 1550 FEG instrument. Water contact angle measurements were performed using the Ossila contact angle Goniometer (L2004A1). EIS was measured by Autolab PGSTAT100, under the dark at a bias of 0.8 V in the frequency range from 500 kHz and 1 Hz with an AC amplitude of 10 mV. Obtained data were analyzed using FRA (frequency response analyzer) 4.5 software. The PL spectra were carried out using a HORIBA Jobin Yvon Fluorolog instrument (Model FL3-222) excitation at 460 nm on the perovskite side. Transient open-circuit voltage decay was measured using a homebuilt system consisting of a white LED (Luxeon Star 1 W) and a digital acquisition board (National Instruments).

Supporting Information

Supporting Information is available from the Wiley Online Library or from the author.

Acknowledgements

S.K.K.A. and A.V. contributed equally to this work. This work was financially supported from Thailand International Cooperation Agency (TICA),

Thailand Science Research and Innovation (TSRI), National Research Council of Thailand (NRCT) from the Royal Golden Jubilee (RGJ) Program, Swedish International Development Cooperation Agency (Sida) and International Science Program (ISP) at Uppsala University under Thai-Swedish Trilateral Development Cooperation Programme (grant no. PHD/0101/2560), the Swedish Foundation for Strategic Research (project no. RMA15-0130), and the Standup for Energy program. The authors thank Kay Thi Soe for XRD characterization.

Conflict of Interest

The authors declare no conflict of interest.

Data Availability Statement

The data that support the findings of this study are available from the corresponding author upon reasonable request.

Keywords

carbon electrodes, lead halide perovskites, poly(3-hexylthiophene), poly(triarylamine)

Received: February 22, 2022
Revised: June 3, 2022
Published online: July 5, 2022

- [1] S. D. Stranks, G. E. Eperon, G. Grancini, C. Menelaou, M. J. P. Alcocer, T. Leijtens, L. M. Herz, A. Petrozza, H. J. Snaith, *Science* **2013**, 342, 341.
- [2] C. Wehrenfennig, G. E. Eperon, M. B. Johnston, H. J. Snaith, L. M. Herz, *Adv. Mater.* **2014**, 26, 1584.
- [3] G. Xing, N. Mathews, S. S. Lim, Y. M. Lam, S. Mhaisalkar, T. C. Sum, *Science* **2013**, 6960, 498.
- [4] B. W. Park, B. Philippe, S. M. Jain, X. Zhang, T. Edvinsson, H. Rensmo, B. Zietz, G. Boschloo, *J. Mater. Chem. A* **2015**, 3, 21760.
- [5] J. You, Z. Hong, Y. M. Yang, Q. Chen, M. Cai, T. Song, C. Chen, S. Lu, Y. Liu, H. Zhou, Y. Yang, *ACS Nano* **2014**, 8, 1674.
- [6] D. Liu, T. L. Kelly, *Nat. Photonics* **2014**, 8, 133.
- [7] J. Jeong, M. Kim, J. Seo, H. Lu, P. Ahlawat, A. Mishra, Y. Yang, M. A. Hope, F. T. Eickemeyer, M. Kim, Y. J. Yoon, I. W. Choi, B. P. Darwich, S. J. Choi, Y. Jo, J. H. Lee, B. Walker, S. M. Zakeeruddin, L. Emsley, U. Rothlisberger, A. Hagfeldt, D. S. Kim, M. Grätzel, J. Y. Kim, *Nature* **2021**, 592, 381.
- [8] P. Roy, N. Kumar Sinha, S. Tiwari, A. Khare, *Sol. Energy* **2020**, 198, 665.
- [9] Y. Rong, Y. Hu, A. Mei, H. Tan, M. I. Saidaminov, S. Il Seok, M. D. McGehee, E. H. Sargent, H. Han, *Science* **2018**, 361, eaat8235.
- [10] S. P. Dunfield, L. Bliss, F. Zhang, J. M. Luther, K. Zhu, M. F. A. M. van Hest, M. O. Reese, J. J. Berry, *Adv. Energy Mater.* **2020**, 10, 1904054.
- [11] G. Tumen-Ulzii, T. Matsushima, C. Adachi, *Energy Fuels* **2021**, 35, 18839.
- [12] G. Ren, W. Han, Y. Deng, W. Wu, Z. Li, J. Guo, H. Bao, C. Liu, W. Guo, *J. Mater. Chem. A* **2021**, 9, 4589.
- [13] S. Kim, S. Bae, S. W. Lee, K. Cho, K. D. Lee, H. Kim, S. Park, G. Kwon, S. W. Ahn, H. M. Lee, Y. Kang, H. S. Lee, D. Kim, *Sci. Rep.* **2017**, 7, 1200.
- [14] G. Tumen-Ulzii, C. Qin, T. Matsushima, M. R. Leyden, U. Balijipalli, D. Klotz, C. Adachi, *Sol. RRL* **2020**, 4, 2000305.
- [15] V. Ferguson, S. R. P. Silva, W. Zhang, *Energy Environ. Mater.* **2019**, 2, 107.
- [16] M. Que, B. Zhang, J. Chen, X. Yin, S. Yun, *Mater. Adv.* **2021**, 2, 5560.
- [17] H. Zhang, K. Song, L. Zhu, Q. Meng, *Carbon N. Y.* **2020**, 168, 372.
- [18] L. Fagiolar, F. Bella, *Energy Environ. Sci.* **2019**, 12, 3437.
- [19] M. Hadadian, J.-H. Småt, J.-P. Correa-Baena, *Energy Environ. Sci.* **2020**, 13, 1377.
- [20] Z. Ku, Y. Rong, M. Xu, T. Liu, H. Han, *Sci. Rep.* **2013**, 3, 3132.
- [21] X. Chen, Y. Xia, Q. Huang, Z. Li, A. Mei, Y. Hu, T. Wang, R. Cheacharoen, Y. Rong, H. Han, *Adv. Energy Mater.* **2021**, 11, 2100292.
- [22] S. M. P. Meroni, W. Caryes, D. Raptis, T. M. Watson, *Energies* **2021**, 14, 386.
- [23] R. He, X. Huang, M. Chee, F. Hao, P. Dong, *Carbon Energy* **2019**, 1, 109.
- [24] E. Calabrò, F. Matteocci, B. Paci, L. Cinà, L. Vesce, J. Barichello, A. Generosi, A. Reale, A. Di Carlo, *ACS Appl. Mater. Interfaces* **2020**, 12, 32536.
- [25] F. Deng, X. Sun, X. Lv, Y. Li, S. Li, Y. Z. Zheng, X. Tao, *J. Power Sources* **2021**, 489, 229345.
- [26] J. Jin, M. Yang, W. Deng, J. Xin, Q. Tai, J. Qian, B. Dong, W. Li, J. Wang, J. Li, *Sol. Energy* **2021**, 220, 491.
- [27] H. Zhou, Y. Shi, K. Wang, Q. Dong, X. Bai, Y. Xing, Y. Du, T. Ma, *J. Phys. Chem. C* **2015**, 119, 4600.
- [28] C. Altinkaya, E. Aydin, E. Ugur, F. H. Isikgor, A. S. Subbiah, M. De Bastiani, J. Liu, A. Babayigit, T. G. Allen, F. Laquai, A. Yildiz, S. De Wolf, *Adv. Mater.* **2021**, 33, 2005504.
- [29] L. Xiong, Y. Guo, J. Wen, H. Liu, G. Yang, P. Qin, G. Fang, *Adv. Funct. Mater.* **2018**, 28, 1802757.
- [30] E. H. Anaraki, A. Kermanpur, L. Steier, K. Domanski, T. Matsui, W. Tress, M. Saliba, A. Abate, M. Grätzel, A. Hagfeldt, J. P. Correa-Baena, *Energy Environ. Sci.* **2016**, 9, 3128.
- [31] J. Yang, B. D. Siempelkamp, E. Mosconi, F. De Angelis, T. L. Kelly, *Chem. Mater.* **2015**, 27, 4229.
- [32] S. Tsarev, S. Olthof, A. G. Boldyreva, S. M. Aldoshin, K. J. Stevenson, P. A. Troshin, *Nano Energy* **2021**, 83, 105774.
- [33] L. Janasz, D. Chlebosz, M. Gradzka, W. Zajaczkowski, T. Marszalek, K. Müllen, J. Ulanski, A. Kiersnowski, W. Pisula, *J. Mater. Chem. C* **2016**, 4, 11488.
- [34] Y. Miyazawa, M. Ikegami, H. W. Chen, T. Ohshima, M. Imaizumi, K. Hirose, T. Miyasaka, *IScience* **2018**, 2, 148.
- [35] E. H. Jung, N. J. Jeon, E. Y. Park, C. S. Moon, T. J. Shin, T. Y. Yang, J. H. Noh, J. Seo, *Nature* **2019**, 567, 511.
- [36] Q. Q. Chu, B. Ding, J. Peng, H. Shen, X. Li, Y. Liu, C. X. Li, C. J. Li, G. J. Yang, T. P. White, K. R. Catchpole, *J. Mater. Sci. Technol.* **2019**, 35, 987.
- [37] S. K. K. Aung, A. Vijayan, T. Seetawan, G. Boschloo, *Sol. RRL* **2021**, 2100773, <https://doi.org/10.1002/solr.202100773>.
- [38] Y. Zou, W. Yu, Z. Tang, X. Li, H. Guo, G. Liu, Q. Zhang, Y. Zhang, Z. Zhang, C. Wu, J. Xiao, B. Qu, Z. Chen, L. Xiao, *Appl. Phys. Lett.* **2021**, 119, 151104.
- [39] M. J. Jeong, K. M. Yeom, S. J. Kim, E. H. Jung, J. H. Noh, *Energy Environ. Sci.* **2021**, 14, 2419.
- [40] H. Wei, J. Xiao, Y. Yang, S. Lv, J. Shi, X. Xu, J. Dong, Y. Luo, D. Li, Q. Meng, *Carbon* **2015**, 93, 861.
- [41] H. Zhang, J. Xiao, J. Shi, H. Su, Y. Luo, D. Li, H. Wu, Y. B. Cheng, Q. Meng, *Adv. Funct. Mater.* **2018**, 28, 1802985.
- [42] H. Su, J. Xiao, Q. Li, C. Peng, X. Zhang, C. Mao, Q. Yao, Y. Lu, Z. Ku, J. Zhong, W. Li, Y. Peng, F. Huang, *Mater. Sci. Semicond. Process.* **2020**, 107, 104809.
- [43] C. Peng, H. Su, J. Li, Q. Duan, Q. Li, J. Xiao, Z. Ku, J. Zhong, W. Li, Y. Peng, F. Huang, *Sol. Energy Mater. Sol. Cells* **2021**, 230, 111226.
- [44] Y. Yang, M. T. Hoang, D. Yao, N. D. Pham, V. T. Tiong, X. Wang, W. Sun, H. Wang, *Sol. Energy Mater. Sol. Cells* **2020**, 210, 110517.

- [45] S. Valastro, E. Smecca, S. Sanzaro, I. Deretzis, A. La Magna, Y. Numata, A. K. Jena, T. Miyasaka, A. Gagliano, A. Alberti, *Front. Chem.* **2020**, *8*, 200.
- [46] V. Babu, R. Fuentes Pineda, T. Ahmad, A. O. Alvarez, L. A. Castriotta, A. Di Carlo, F. Fabregat-Santiago, K. Wojciechowski, *ACS Appl. Energy Mater.* **2020**, *3*, 5126.
- [47] S. M. P. Meroni, K. E. A. Hooper, T. Dunlop, J. A. Baker, D. Worsley, C. Charbonneau, T. M. Watson, *Energies* **2020**, *13*, 1589.
- [48] H. Zhou, Y. Shi, Q. Dong, H. Zhang, Y. Xing, K. Wang, Y. Du, T. Ma, *J. Phys. Chem. Lett.* **2014**, *5*, 3241.
- [49] F. Behrouznejad, M. Forouzandeh, R. Khosroshahi, K. Meraji, M. N. Badrabad, M. Dehghani, X. Li, Y. Zhan, Y. Liao, Z. Ning, N. Taghavinia, *Sol. RRL* **2020**, *4*, 1900564.
- [50] J. Han, X. Yin, Y. Zhou, H. Nan, Y. Gu, M. Tai, J. Li, H. Lin, *ACS Appl. Mater. Interfaces* **2018**, *10*, 42328.
- [51] S. Nair, J. V. Gohel, *Opt. Mater.* **2021**, *119*, 111366.
- [52] H. Xie, J. Liu, X. Yin, Y. Guo, D. Liu, G. Wang, W. Que, *Colloids Surf. A Physicochem. Eng. Asp.* **2022**, *635*, 128072.
- [53] H. Xiong, G. Deluca, Y. Rui, B. Zhang, Y. Li, Q. Zhang, H. Wang, E. Reichmanis, *ACS Appl. Mater. Interfaces* **2018**, *10*, 35385.
- [54] K. Mantulnikovs, A. Glushkova, P. Matus, L. Ćirić, M. Kollár, L. Forró, E. Horváth, A. Sienkiewicz, *ACS Photonics* **2018**, *5*, 1476.
- [55] M. Jiang, J. Yuan, G. Cao, J. Tian, *Chem. Eng. J.* **2020**, *402*, 126152.
- [56] N. K. Noel, A. Abate, S. D. Stranks, E. S. Parrott, V. M. Burlakov, A. Goriely, H. J. Snaith, *ACS Nano* **2014**, *8*, 9815.
- [57] J. Li, J. X. Yao, X. Y. Liao, R. L. Yu, H. R. Xia, W. T. Sun, L. M. Peng, *RSC Adv.* **2017**, *7*, 20732.
- [58] S. Wang, H. Liu, H. Bala, B. Zong, L. Huang, *Electrochim. Acta* **2020**, *335*, 135686.
- [59] T. Xu, K. Zou, S. Lv, H. Tang, Y. Zhang, Y. Chen, L. Chen, Z. Li, W. Huang, *ACS Appl. Mater. Interfaces* **2021**, *13*, 16485.